LETTER

Zwitterionic Bifunctional Layer for Reversible Zn Anode

Renpeng Chen,[§] Qin Liu,[§] Lin Xu,* Xuri Zuo, Fang Liu, Jianyong Zhang, Xuan Zhou, and Liqiang Mai*

Read Online

ACCESS | Metrics & More | Article Recommendations | SI Supporting Information

ABSTRACT: A Zn metal anode suffers from severe dendrite issues and passive byproducts, which restrict the practical application of Zn-ion batteries. Herein, a bifunctional poly zwitterionic ionic liquid (PZIL) is designed as a new ion-migration layer to suppress Zn dendrites and side reactions. On one hand, the zwitterionic functional groups on the PZIL layer guide the Zn ion distribution to regulate the deposition behavior of Zn. On the other hand, the tight bond between zwitterionic groups and water molecules can build an H_2O-poor interface on the surface of the Zn anode to avoid side reactions. Based on the above two functions, a symmetrical cell with the PZIL-layer-modified Zn exhibits a stable plating/stripping performance (2600 h at 1 mA cm^{-2}) with low reversible deposition potential (∼50 mV). The concept of a zwitterionic bifunctional layer will open up a new avenue for reversible anodes for Zn-ion batteries as well as other battery systems.
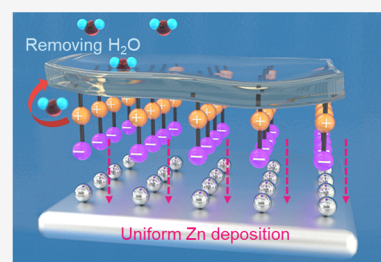
Lithium-ion batteries (LIBs) are widely used in electric vehicles, mobile electronic device, and the internet of things.[1−3] However, explosions and fires of rechargeable LIBs have occurred frequently in recent years.[4] The flammability of organic electrolytes hinders the further development of LIBs.[5,6] Rechargeable aqueous batteries have attracted tremendous attention because of their high safety, low cost, and environmental benignity.[7] Among them, aqueous Zn-ion batteries (ZIBs) are the most powerful candidate owing to the high theoretical specific capacity (820 mAh g^{-1} or 5855 mAh cm^{-3}) of Zn metal.[8−10] Nevertheless, the unstable zinc anode seriously hinders the long-term cycling of ZIBs.[11] First, uncontrolled growth of Zn dendrites is generated by inhomogeneous charge concentration and nucleation. The nucleation of Zn ions tends to occur at lower-energy positions, thereby leading to uneven Zn dendrites and broken "dead Zn", resulting in a decrease in the Coulomb efficiency (CE) (Figure 1a).[12−14] Second, Zn metal is thermodynamically unstable in aqueous electrolytes, easily reacting with water and oxygen dissolved in an aqueous environment, producing large amounts of byproducts such as $Zn_4(OH)_6SO_4 \cdot xH_2O$.[15−17] Third, the accumulation of dendrites and byproducts will expand the contact area between electrolytes and Zn anode, which exacerbates the negative reaction. Therefore, the passive side reaction between Zn anode and aqueous electrolyte leads to poor reversibility of plating/stripping, accompanied by Zn dendrite growth.[18] Further, the continued growth of Zn dendrites will pierce the separator, which will cause a short circuit and failure of the battery.[19]

In response, several strategies have been developed to solve the aforementioned issues. The construction of a three-dimensional (3D) electrode structure is a classical design, which can regulate the flux of Zn ions to promote the uniform deposition.[20,21] Another approach is the modification of electrolytes, including high-concentration electrolyte,[22] introduction of electrolyte additives,[23] construction of (quasi-) solid-state electrolytes,[24] eutectic electrolytes,[25] etc. Despite the enhanced reversibility of the Zn anode, the complicated preparation processes and high cost still inhibit the commercial application of ZIBs. As a possible low-cost and scalable strategy, the construction of a functional layer on the surface of metal Zn is more practical.[26] At present, inorganic coatings such as graphene,[27] metal nanoparticles,[28] and inorganic nanoparticles[29] have been extensively studied. However, the weak adsorption and brittleness of the inorganic coating layer make it fall off easily when the Zn anode undergoes repeated plating/stripping cycles, leading to volume expansion. It is a feasible strategy to combine organic and inorganic materials to improve the adhesion and mechanical adaptability of the protective layer.[30−32] Unfortunately, poor dispersion of nanoscale particles is not conducive to its uniform distribution in the coating layer, which leads to the failure of precise and
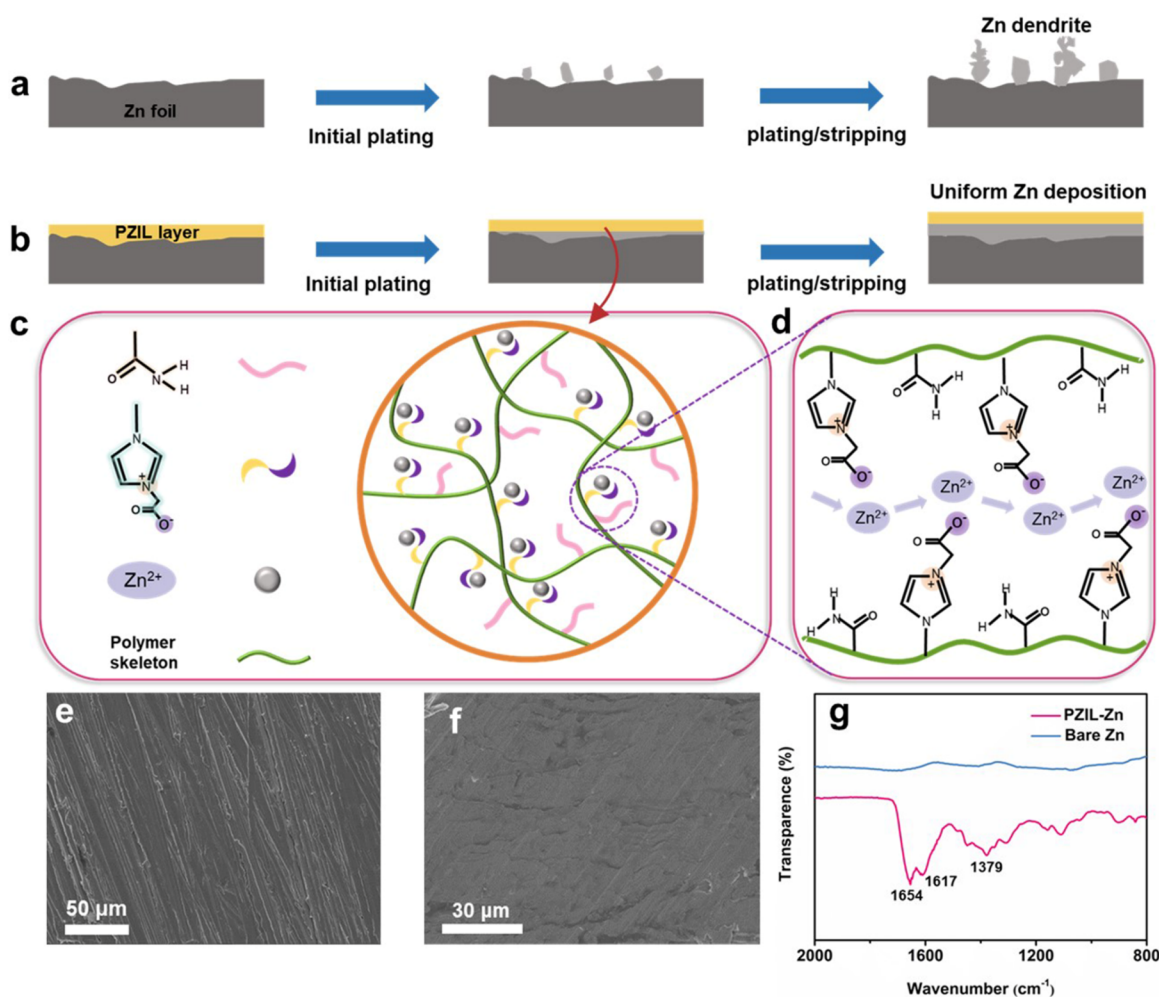
Figure 1. (a and b) Schematic diagrams for the repeated Zn stripping/plating of bare Zn and PZIL-Zn anode. (c) Chemical structure of PZIL. (d) Ion regulation mechanism of PZIL in electrolyte. SEM images of (e) bare Zn and (f) PZIL-coated Zn foil. (g) FTIR spectrum of the bare Zn and PZIL layer on the surface of Zn metal.

uniform Zn ion transport. These challenges and problems will eventually spur us to develop a simple and effective method to accurately regulate the anode/electrolyte interface to construct stable Zn anode.

Herein, we developed a bifunctional poly-zwitterionic ionic liquid (PZIL) ion-migration layer that can prevent dendrite growth and inhibit corrosion reactions to stabilize the Zn metal anode surface. The PZIL artificial protective layer, formed by free-radical copolymerization of 1-vinyl-3-(carboxymethyl)-imidazolium and acrylamide (AM), is prepared on the surface of Zn foil (denoted as PZIL-Zn). The three-dimensional (3D) porous network structure of the PZIL prevents the coating layer from dissolving in the aqueous electrolyte. Furthermore, the oxygen-containing functional groups on the polymer chain segment result in a strong adhesion to Zn metal during the electrochemical process. On one hand, the PZIL functional layer can hinder the direct contact between the electrolyte and the Zn anode, attributed to the strong attraction between zwitterionic groups and water molecules, which effectively promotes the desolvation process and prevents the corrosion of the Zn metal anode. On the other hand, the anions on the zwitterionic chains facilitate the uniform distribution of Zn ions as proved by density functional theory (DFT) calculation. The Zn ions are uniformly deposited on the surface of Zn metal, thereby preventing the rampant growth of Zn dendrites

(Figure 1b). Because of these unique two functions, the PZIL-Zn delivers longer cyclability of 2600 h at 1 mA cm^{-2} and higher average CE of 99.65% for 1000 cycles. The full cell coupled with a manganese dioxide cathode also shows an excellent stability, demonstrating a promising method for constructing high-performance aqueous Zn batteries.

To prepare the artificial coating layer, acrylamide and 1-vinyl-3-(carboxymethyl)-imidazolium monomer were first dissolved in an aqueous solution to prepare a precursor solution, and then, the precursor solution was uniformly spin-coated on the Zn foil followed by free-radical polymerization. As an ion regulatory layer, the role of PZIL is conceptually illustrated in Figure 1c,d. The deposition behavior on Zn foil can be effectively regulated by the strong binding force between zwitterionic functional groups and Zn ions. The surface morphology of bare Zn and PZIL-Zn was observed from scanning electron microscopy (SEM) (Figure 1e,f and Figure S1). Compared with bare Zn, the PZIL-Zn foil presented a dense surface. Meanwhile, the surface coating layer was characterized by the Fourier transform infrared spectroscopy (FTIR) spectrum. As shown in Figure 1g, the typical overlap bands at 1654 and 1617 cm^{-1} are attributed to the amide group of AM and C=O group of ZIL.[33] The imidazole group shifted to 1379 cm^{-1}, indicating that there are ionic associations between the imidazole and the −COO$^-$
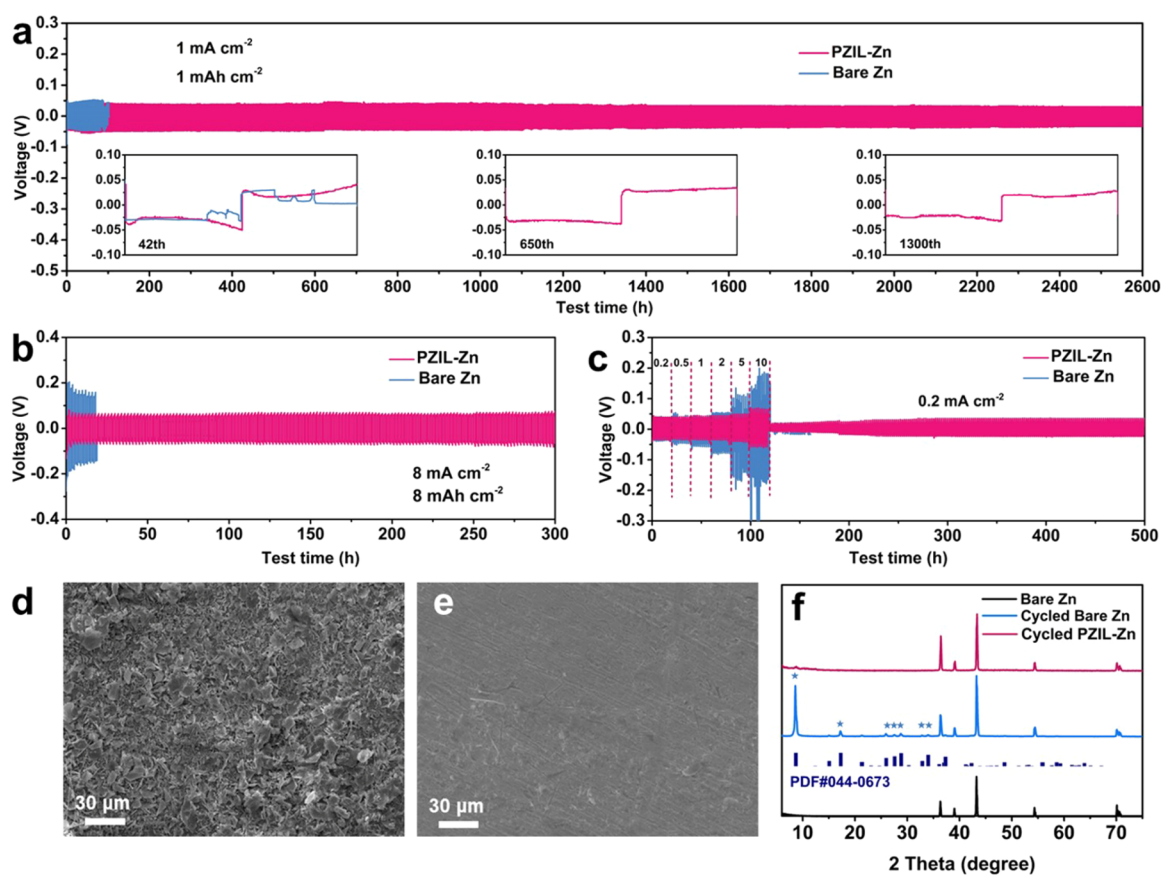
Figure 2. Zn plating/stripping performance for bare Zn metal and PZIL-Zn metal. (a) The long cycling performance of symmetrical bare Zn and PZIL-Zn cell at a current density of 1 mA cm^{-2}. (b) The cycling performance of symmetrical cell at a high current density of 8 mA cm^{-2} and (c) various current densities. SEM images of (d) bare Zn and (e) PZIL-Zn after striping/plating for 100 cycles at 1 mA cm^{-2} and 1 mAh cm^{-2}. (f) XRD patterns of the cycled bare and PZIL-Zn (the corresponding JCPDS files: PDF 44-0673 for Zn$_4$SO$_4$(OH)$_6$·4H$_2$O).

group. There is no characteristic peak of C=C observed in the Raman spectrum of the PZIL layer, which indicates a high degree of polymerization reaction (Figure S2). Then, the PZIL layer on Zn foil was also characterized by X-ray photoelectron spectroscopy (XPS). The peak at 401.7 eV corresponded to the N$^+$ in the imidazolium moiety, which proves successful conversion of the imidazole moiety into the imidazolium moiety.[34] Meanwhile, the characteristic peaks of C−C, C−O, and C=O could be observed in C 1s, and C=O and C−O could also be observed in O 1s, suggesting the existence of the PZIL artificial interface layer (Figure S3).[35]

To explore the protective ability of the PZIL layer on the Zn foil, bare Zn and PZIL-Zn were soaked in 2 M ZnSO$_4$ solution for 10 days. The rough surface occurred on bare Zn after immersion, and a large number of flakes were observed from SEM images, indicating that unprotected Zn metal would produce undesirable side reactions in the ZnSO$_4$ electrolyte due to the corrosion of H$_2$O/O$_2$ (Figure S4).[36] The Zn foil protected by PZIL still maintained the metallic luster, and no metal flakes were observed. Further, the anticorrosion properties of the PZIL layer were analyzed by Tafel fitting of linear polarization curves (Figure S5). Compared with bare Zn (5.28 mA cm^{-2}), the corrosion current of PAM-Zn and PZIL-Zn decreased to 3.17 and 2.24 mA cm^{-2}, respectively, suggesting a lower corrosion rate. In addition, the corrosion potential of PZIL-Zn increased, suggesting less electrochemical corrosion tendency.[37] Meanwhile, the effect of the modified layer on hydrogen evolution can be studied by corrosion

curves (Figure S6). PZIL-Zn shows the higher potential of hydrogen evolution reaction in comparison to that of bare Zn, reflecting the hydrogen suppression.

The electrochemical stability of the Zn anode was evaluated by repeated plating/stripping of Zn in 2 M ZnSO$_4$ solution. The voltage of bare Zn suddenly drops at 84 h at a current density/deposited amount of 1 mA cm^{-2}/1 mAh cm^{-2}, which means that a short circuit occurred on the cell. In contrast, the PZIL-Zn exhibited stable polarization voltage and long plating/stripping for 2600 h (Figure 2a). The PZIL-Zn shows higher reversible ability than other reports (Table S1, Supporting Information). PZIL-Zn still showed better electrochemical stability than bare Zn when the current density was increased to 5 mA cm^{-2} (Figure S7). Even when the current density/deposition amount was increased to 8 mA cm^{-2}/8 mAh cm^{-2}, PZIL-Zn could maintain stable polarization for 300 h (Figure 2b), whereas bare Zn could not withstand the high current density, and a short circuit occurred soon. The rate stability of PZIL-Zn under different currents was also confirmed, where the PZIL-Zn exhibited great rate performance, but the polarization voltage of bare Zn rose strikingly at 5 mA cm^{-2} (Figure 2c). Meanwhile, Figure S8 shows the EIS curves of PZIL-Zn and bare Zn after 100 cycles; a slight decrease in impedance indicates better interfacial contact and ion transport. In contrast, the symmetrical battery composed of bare Zn failed (Figure S8). The reason for the cell failure may be the massive growth of Zn dendrites, which will eventually pierce the separator. The irregular accumulation of dendrites
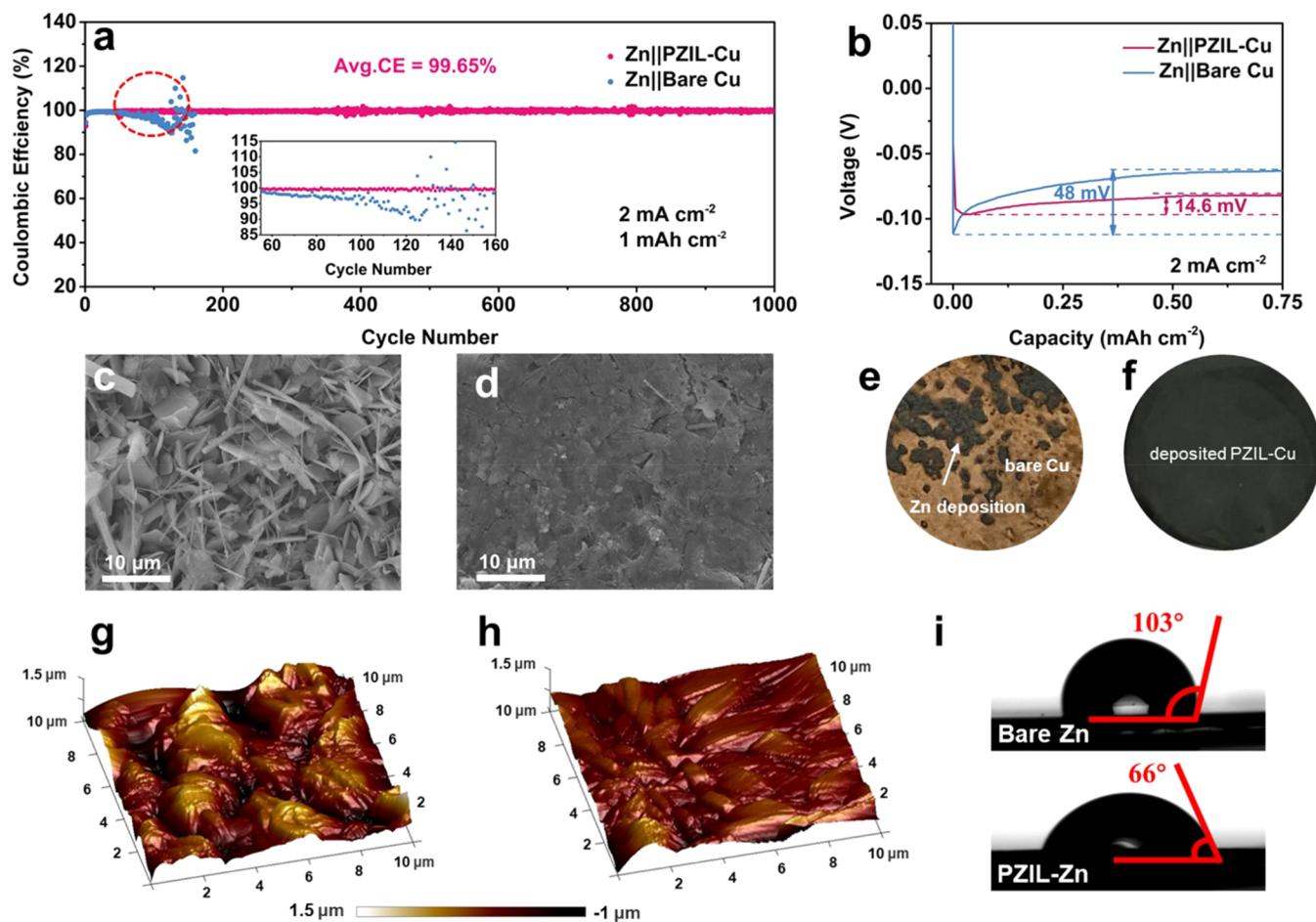
Figure 3. (a) CE tests of Zn||Cu and Zn||PZIL-Cu at a current density of 2 mA cm^{-2}. (b) Overpotentials of Zn deposition on the bare Cu and PZIL-Cu. (c and d) SEM images of bare Cu and PZIL-Cu after plating Zn at 2 mA cm^{-2} and 4 mAh cm^{-2}. (e) Digital photo of deposited bare Cu showed a rough surface, and (f) a uniform surface was observed on deposited PZIL-Cu. AFM images of (g) the bare Cu and (h) PZIL-Cu electrodes after plating 1 mAh cm^{-2} Zn. (i) Static contact angle of 2 M ZnSO$_4$ electrolyte on bare Zn and PZIL-Zn.

was confirmed from the SEM image of the cycled bare Zn. But the cycled PZIL-Zn showed a smooth surface, and no obvious Zn dendrites were observed (Figure 2d,e). It is worth noting that the polarization voltage of poly acrylamide coated Zn foil (denoted as PAM-Zn) gradually increased during the cycle (Figure S9). This may be the result of the formation of a large amount of Zn dendrites and insulation byproducts (Figure S10). In particular, the byproducts are caused by the direct contact of H$_2$O/O$_2$ and SO$_4$$^{2-}$ with Zn foil in aqueous electrolyte. By contrast, the zwitterionic ions in PZIL feature stronger adsorption effect on H$_2$O molecules, preventing direct contact between water and Zn foil. Further verified by X-ray diffraction (XRD), cycled bare Zn showed an obvious byproduct peak of Zn$_4$(OH)$_6$SO$_4$·4H$_2$O (PDF 044-0673), while PZIL-Zn can exhibit only a weak peak (Figure 2f).

In order to explore the reversibility of Zn plating/stripping, the CE was tested by a Zn||Cu cell in 2 M ZnSO$_4$ electrolytes. The PZIL layer was coated on the Cu foil by the same in situ polymerization method (denoted as PZIL-Cu). Subsequently, 1 mAh cm^{-2} of Zn was plated on Cu or PZIL-Cu, and then stripped from the Cu substrate. During each testing cycle, the CE was calculated by the ratio of the amount of the stripping Zn to plating Zn. At a current density of 2 mA cm^{-2}, Zn||PZIL-Cu exhibited stable plating/stripping of Zn for 1000 cycles and the average CE was still as high as 99.65% (Figure 3a).

Unfortunately, the CE of the Zn||Cu cell decreased after plating/stripping for about 50 cycles, and finally failed after 120 cycles. PAM coating layers with zwitterionic functional groups also showed a similar tendency of CE decay (Figure S11). The reduction of CE is mainly due to the side reaction and the accumulation of dendritic dendrites. The nucleation overpotential of PZIL-Cu was only 14.6 mV, which was much lower than the 48 mV of bare Cu (Figure 3b), meaning that the PZIL layer provided more nucleation sites and promoted the uniform nucleation of Zn ions. This was also confirmed by the morphology of cycled PZIL-Cu and bare Cu. The bare Cu exhibited a surface of rough dendrites with a large number of glass fibers (Figure 3c), suggesting the accumulation of Zn dendrites piercing into the separator. In contrast, except for a small amount of glass fiber thread, a flat and dendrite-free surface on PZIL-Cu was observed (Figure 3d). The deposited surface was visually observed on digital photos of PZIL-Cu and bare Cu; the Zn was uniformly deposited on the surface of PZIL-Cu, but the uneven surface was clearly observed on bare Cu (Figure 3e,f). Furthermore, atomic force microscopy (AFM) was conducted to quantify the corresponding 3D height (Figure 3g,h). The deposited PZIL-Cu showed a height fluctuation smaller than that of deposited bare Cu.

The nonuniform wetting between the electrolyte and the Zn electrode will cause uneven distribution of surface charges,
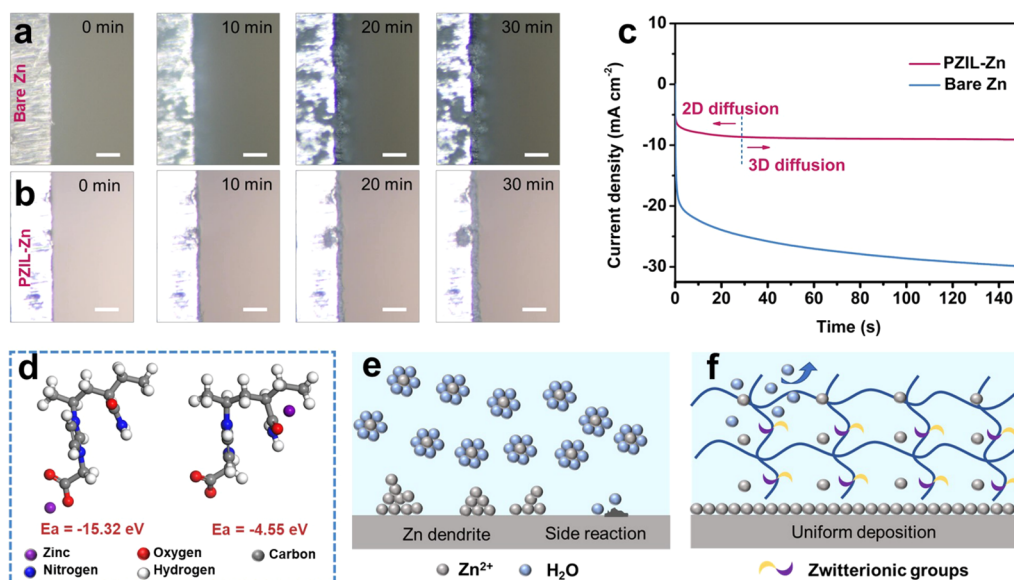
Figure 4. (a and b) In situ optical microscopy of Zn plating on bare Zn and PZIL-Zn at 5 mA cm^{-2} for 30 min. Scale bar: 50 μm. (c) CAs of the bare Zn and PZIL-Zn under −150 mV overpotential. (d) DFT calculation models for binding energy of Zn absorbed on PZIL with different groups. Schematic diagrams of the Zn plating behavior on (e) bare Zn and (f) PZIL-Zn.

resulting in disorderly electrodeposition. The hydrophilicity of the PZIL layer was tested through measuring the static contact angle. The contact angle of 2 M ZnSO$_4$ on the bare Zn was 103°, while the contact angles on PAM-Zn and PZIL-Zn are 84° and 66°, respectively (Figures 3i and S12). It is indicated that the artificial functional layer significantly enhanced the hydrophilicity because of its abundant polar functional groups.[38] Considering the thermodynamics, the enhancement of hydrophilicity reduces the free energy of the interfaces between the electrolyte and the Zn electrode, suggesting that fast ion transfer exists at the interface between electrolyte and PZIL-Zn. This was also confirmed from the electrochemical impedance spectroscopy (EIS) measurements (Figure S13). The symmetric cells of PZIL-Zn with better hydrophilicity exhibited lower charge-transfer resistance than bare Zn under different temperatures. Meanwhile, the corresponding activation energy was calculated through the Arrhenius equation.[39] The activation energy of PZIL-Zn was 22.56 kJ mol^{-1}, while that of bare Zn was 25.58 kJ mol^{-1}, further proving that the PZIL protective layer promoted the desolvation process and the transfer of Zn^{2+} (Figure S14).

In order to observe the deposition process of Zn foil (bare Zn and PZIL-Zn) more intuitively, the in situ growth process of Zn was observed through an optical microscope. The deposition continued for 30 min at a current density of 5 mA cm^{-2}. Figure 4a shows that uneven Zn deposition appeared on the bare Zn foil after deposition for 10 min. As the deposition time further increased to 30 min, sharp tree-like Zn dendrites could be observed. Such dendritic Zn may pierce the separator and bridge the electrodes, resulting in short circuits. For PZIL-Zn, no random growth of Zn dendrites was observed (Figure 4b), indicating that the Zn was uniformly deposited under the PZIL layer. This further confirms that a large number of nucleation sites and uniform electric field distribution on PZIL-Zn induce the uniform deposition of Zn ion. In order to prove that the protective layer could stably adhere to the surface of the Zn foil during the process of plating/stripping. The cross section of the cycled PZIL-Zn foil was observed.

The protective layer stably existed on the surface of the Zn electrode, and plating Zn was evenly distributed under the PZIL layer (Figure S15).

The deposition mechanism of Zn on the coating layer was scrutinized by chronoamperometry (CA). The test method reflects the changes of surface morphology by fluctuation of the current−time profile during the nucleation process. With an overpotential of −150 mV applied, the current of bare Zn increased continuously within 150 s, indicating a long and unordered 2D diffusion during this period.[40] Zn ions tend to diffuse laterally along the surface, deposit at the most favorable energy position, and finally grow into rampant dendrites. In contrast, the initial 2D diffusion of Zn ions on PZIL-Zn occurred within 30 s, followed by a stable 3D diffusion during the subsequent process (Figure 4c). The deposition of Zn ions occurred near the initial adsorption sites, resulting in the increase of nucleation sites. This is attributed to the existence of polar groups in the coating layer, forming a continuous ion channel to make the nucleation of Zn ions denser. Moreover, density functional theory (DFT) calculations were implemented to further explore the role of the polar functional group on the PZIL layer in regulating Zn deposition. Figure 4d shows the configuration of segments of PZIL with Zn salt. The binding energy of −COO$^-$Zn^{2+} (−15.32 eV) is higher than that of the acyl group (−4.55 eV), indicating that Zn^{2+} was inclined to combine with −COO$^-$. Further, the binding energy of −COO$^-$ and Zn$^+$ is also higher than that of Zn−H$_2$O (−9.59 eV), indicating that Zn^{2+} will be captured by −COO$^-$ instead of water (Figure S16). The solvation structure of PZIL in ZnSO$_4$ solutions was observed via Raman spectra. The O−H stretching region of H$_2$O in Raman spectra shows two characteristic peaks at 3405 and 3220 cm^{-1} related to free water and bound water, respectively. The higher intensity of 3405 cm^{-1} indicated an increase in free water, suggesting that PZIL changed the solvation shell structure of water and Zn ions (Figure S17).[41] Therefore, the introduction of zwitterion groups provides abundant Zn-oriented groups to promote the uniform transfer of Zn ions and promotes the desolvation
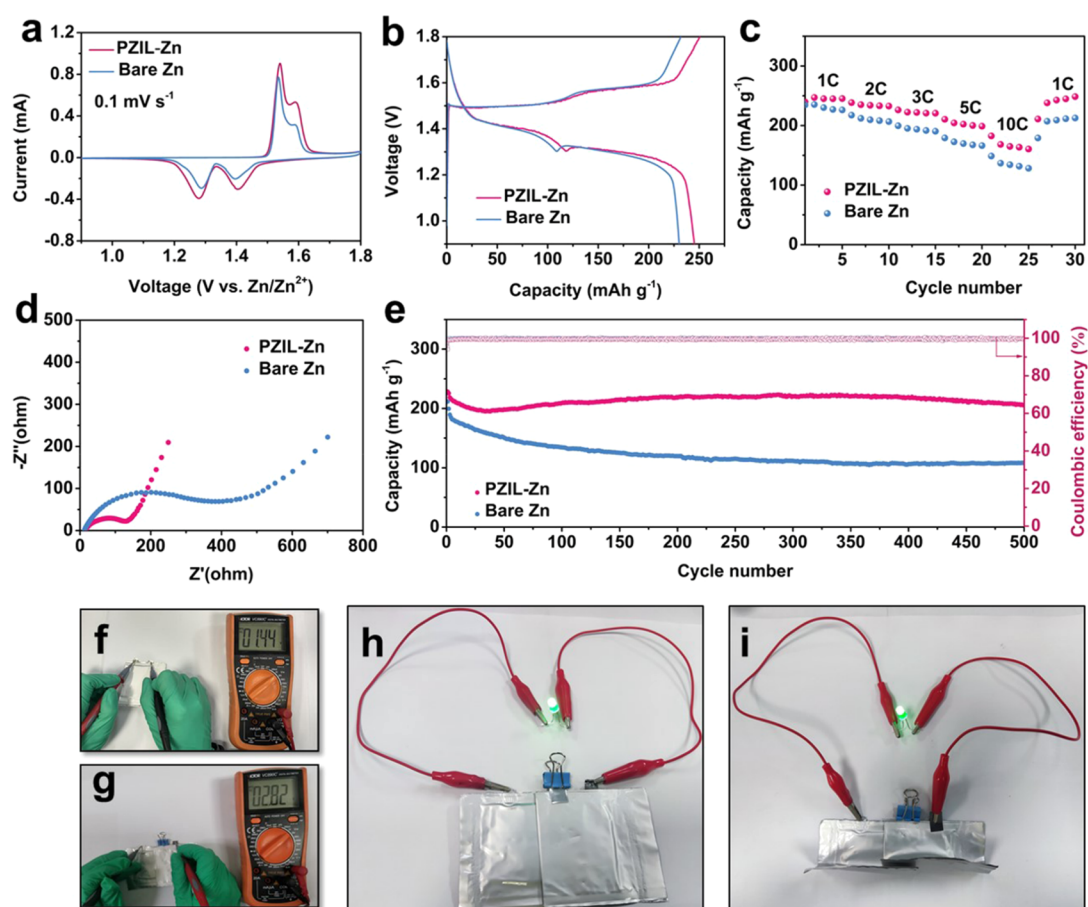
Figure 5. Electrochemical performance of full cell with bare Zn anode and PZIL-Zn anode. (a) CV measurement at 0.1 mV s^{-1}. (b) Charge/discharge curves at 1C. (c) Rate performance. (d) EIS curves of full cell with PZIL-Zn or bare Zn. (e) Long-term cycling performance at 3C after 500 cycles. (f) Digital photo of open-circuit voltage of the soft-packaged and (g) two soft-packaged in series. (h) Digital photo showing the working states of PZIL-Zn soft-packaged in series to power a LED indicator. (i) Digital photo of PZIL-Zn soft-packaged cells in series after being bent.

process. According to the theoretical analysis provided above, the schematic diagram of the PZIL layer functional mechanism is shown in Figure 4f. The uneven nucleation sites on bare Zn foil will promote the disorderly growth of dendrites, and the Zn foil is in direct contact with H_2O molecules, resulting in a corrosion reaction (Figure 4e). In contrast, the PZIL layer promotes the desolvation process. On the one hand, the zwitterion will change the solvation structure of the hydrated Zn^{2+}, which will reduce the number of water molecules around the Zn ion, and fewer water molecules will be in direct contact with the Zn anode; on the other hand, the free water in the interface layer can be tightly bound to the zwitterionic groups because of charge–dipole and dipole–dipole interaction performance, thereby suppressing the diffusion behavior of free water. The dense and negatively charged network structure of the PZIL layer produces abundant nucleation sites, causing the formation of a dendrite-free Zn metal anode.

The practical application of PZIL-Zn was further verified by assembling full cells using MnO_2/CNT as cathode. The cathode was fabricated by a hydrothermal method, and the morphology and purity of the cathode material was checked by SEM and XRD characterization (Figure S18,19). In order to fit the cathode material, 0.2 M $MnSO_4$ was added to the 2 M $ZnSO_4$ to inhibit the disproportionation reaction of the cathode material. Cyclic voltammogram (CV) curves of the full cell assembled by bare Zn and PZIL-Zn were tested at a

scan rate of 0.1 mV s^{-1}, presenting the typical two pairs of redox peaks (Figure 5a). The two redox peaks are attributed to Zn^{2+} or H^+ insertion/extraction reactions.[42,43] Meanwhile, the charge/discharge curves of the full battery were consistent with the CV curves (Figure 5b). The rate performance of the full cells at various current densities (0.5 to 10 C, 1 C = 308 mA g^{-1}) has been examined (Figure 5c). Even at the high current density of 10 C, the capacity of the PZIL-Zn full cell can still maintain 168 mAh g^{-1} and back to 238 mAh g^{-1} at 1 C, corresponding to the charge/discharge curves at different current densities (Figure S20). However, the capacity of the full battery assembled by bare Zn showed a significantly lower capacity than that of PZIL-Zn. The superior capacities of PZIL-Zn full battery in various current densities suggested that the fast ion transport of the PZIL layer, which could be confirmed from the lower impedance of the PZIL-Zn full cell (Figure 5d). Finally, the long cycling performance of PZIL-Zn full battery was tested at a current density of 3 C. The full cell of the PZIL-Zn anode showed high capacity of 205 mAh g^{-1} after 500 cycles (Figure 5e). However, the discharge capacity of bare Zn full cell decreased to 108 mAh g^{-1}. The low-capacity retention of the bare Zn full battery was attributed to the electrochemical corrosion and the accumulation of dendrites on bare Zn (Figure S21).

In order to demonstrate a practical application, PZIL-Zn was assembled into soft-packaged batteries. A soft-packaged battery

with PZIL-Zn showed a stable open-circuit voltage, and the two soft-packaged batteries could be connected in series (Figure 5f,g). The soft-packaged batteries in series made a light-emitting diode (LED) indicator work successfully under bending, suggesting the PZIL-Zn is intrinsically flexible (Figure 5h,i). The PZIL-Zn soft-packaged batteries also could power the LED indicator after being cut (Figure S22). All the above results show that the PZIL layer can effectively suppress dendrite protuberances and the side reactions between the Zn anode and electrolyte, which is conducive to the superior electrochemical performance of ZIBs.

In conclusion, a PZIL layer with zwitterionic bifunctional groups haa been fabricated on Zn foil by in situ polymerization. The ion transport between electrolytes and Zn anode can be regulated by zwitterionic groups to increase the nucleation site to refine the nucleation grains. In addition, the strong binding force between zwitterionic functional groups and water can effectively inhibit the direct contact between water molecules in the electrolyte and the Zn anode. The reduction of the side reaction and uniform nucleation of Zn ions assist in the construction of the reversible Zn anode. As a result, a long cycling life of Zn plating/stripping is up to 2600 h at 1 mA cm^{-2}, along with a low deposition potential of ∼50 mV. The reversible plating/stripping of Zn on PZIL-Cu is up to 1000 cycles with a high average CE of 99.65%. More importantly, the full battery still maintains 205 mAh g^{-1} and high capacity retention of 90% after 500 cycles. This facile zwitterionic bifunctional layer promotes dendrite-free metal electrodeposition, and the in-depth understanding of the mechanism provides a fresh perspective on next-generation aqueous batteries.

■ ASSOCIATED CONTENT

Ⓢ Supporting Information

The Supporting Information is available free of charge at https://pubs.acs.org/doi/10.1021/acsenergylett.2c00124.

> Additional experimental details including Figures S1−S22 and Table S1; computational and experimental methods; DFT simulation results; optical images; Raman spectra; FTIR spectra; XRD patterns; SEM images; XPS spectra; and additional electrochemical data (PDF)

■ AUTHOR INFORMATION

Corresponding Authors

Lin Xu − *State Key Laboratory of Advanced Technology for Materials Synthesis and Processing, School of Materials Science and Engineering, Wuhan University of Technology, Wuhan 430070 Hubei, P.R. China; Foshan Xianhu Laboratory of the Advanced Energy Science and Technology Guangdong Laboratory, Xianhu Hydrogen Valley, Foshan 528200 Guangdong, P.R. China;* ⓞ orcid.org/0000-0003-2347-288X; Email: linxu@whut.edu.cn

Liqiang Mai − *State Key Laboratory of Advanced Technology for Materials Synthesis and Processing, School of Materials Science and Engineering, Wuhan University of Technology, Wuhan 430070 Hubei, P.R. China; Foshan Xianhu Laboratory of the Advanced Energy Science and Technology Guangdong Laboratory, Xianhu Hydrogen Valley, Foshan 528200 Guangdong, P.R. China;* ⓞ orcid.org/0000-0003-4259-7725; Email: mlq518@whut.edu.cn

Authors

Renpeng Chen − *State Key Laboratory of Advanced Technology for Materials Synthesis and Processing, School of Materials Science and Engineering, Wuhan University of Technology, Wuhan 430070 Hubei, P.R. China*

Qin Liu − *State Key Laboratory of Advanced Technology for Materials Synthesis and Processing, School of Materials Science and Engineering, Wuhan University of Technology, Wuhan 430070 Hubei, P.R. China*

Xuri Zuo − *State Key Laboratory of Advanced Technology for Materials Synthesis and Processing, School of Materials Science and Engineering, Wuhan University of Technology, Wuhan 430070 Hubei, P.R. China*

Fang Liu − *State Key Laboratory of Advanced Technology for Materials Synthesis and Processing, School of Materials Science and Engineering, Wuhan University of Technology, Wuhan 430070 Hubei, P.R. China*

Jianyong Zhang − *State Key Laboratory of Advanced Technology for Materials Synthesis and Processing, School of Materials Science and Engineering, Wuhan University of Technology, Wuhan 430070 Hubei, P.R. China*

Xuan Zhou − *State Key Laboratory of Advanced Technology for Materials Synthesis and Processing, School of Materials Science and Engineering, Wuhan University of Technology, Wuhan 430070 Hubei, P.R. China*

Complete contact information is available at:
https://pubs.acs.org/10.1021/acsenergylett.2c00124

Author Contributions

§R.C. and Q.L. contributed equally to this work.

Notes

The authors declare no competing financial interest.

■ ACKNOWLEDGMENTS

■ REFERENCES

(1) Manthiram, A.; Yu, X.; Wang, S. Lithium battery chemistries enabled by solid-state electrolytes. *Nat. Rev. Mater.* **2017**, *2* (4), 16103.

(2) Han, C.; Li, H.; Li, Y.; Zhu, J.; Zhi, C. Proton-assisted calcium-ion storage in aromatic organic molecular crystal with coplanar stacked structure. *Nat. Commun.* **2021**, *12*, 2400.

(3) Yan, M.; Zhao, Y.; Mai, L. Track batteries degrading in real time. *Nature* **2017**, *546*, 469−470.

(4) Konarov, A.; Voronina, N.; Jo, J. H.; Bakenov, Z.; Sun, Y.-K.; Myung, S.-T. Present and Future Perspective on Electrode Materials for Rechargeable Zinc-Ion Batteries. *ACS Energy Lett.* **2018**, *3* (10), 2620−2640.

(5) Zhao, Q.; Stalin, S.; Zhao, C.-Z.; Archer, L. A. Designing solid-state electrolytes for safe, energy-dense batteries. *Nat. Rev. Mater.* **2020**, *5* (3), 229−252.

(6) Fang, G.; Zhou, J.; Pan, A.; Liang, S. Recent Advances in Aqueous Zinc-Ion Batteries. *ACS Energy Lett.* **2018**, *3* (10), 2480−2501.

(7) Han, C.; Zhang, T.; Li, J.; Li, B.; Lin, Z. Enabling flexible solid-state Zn batteries via tailoring sulfur deficiency in bimetallic sulfide nanotube arrays. *Nano Energy* **2020**, *77*, 105165.

(8) Tang, Z.; Chen, W.; Lyu, Z.; Chen, Q. Size-Dependent Reaction Mechanism of λ-MnO$_2$ Particles as Cathodes in Aqueous Zinc-Ion Batteries. *Energy Material Advances* **2022**, *2022*, 1−12.

(9) Li, H.; Han, C.; Huang, Y.; Huang, Y.; Zhu, M.; Pei, Z.; Xue, Q.; Wang, Z.; Liu, Z.; Tang, Z.; Wang, Y.; Kang, F.; Li, B.; Zhi, C. An extremely safe and wearable solid-state zinc ion battery based on a hierarchical structured polymer electrolyte. *Energy Environ. Sci.* **2018**, *11* (4), 941−951.

(10) Wan, F.; Zhou, X.; Lu, Y.; Niu, Z.; Chen, J. Energy Storage Chemistry in Aqueous Zinc Metal Batteries. *ACS Energy Lett.* **2020**, *5* (11), 3569−3590.

(11) Zhang, Y.; Howe, J. D.; Ben-Yoseph, S.; Wu, Y.; Liu, N. Unveiling the Origin of Alloy-Seeded and Nondendritic Growth of Zn for Rechargeable Aqueous Zn Batteries. *ACS Energy Lett.* **2021**, *6* (2), 404−412.

(12) Wang, K.; Pei, P.; Ma, Z.; Chen, H.; Xu, H.; Chen, D.; Wang, X. Dendrite growth in the recharging process of zinc−air batteries. *J. Mater. Chem. A* **2015**, *3* (45), 22648−22655.

(13) Yang, Q.; Liang, G.; Guo, Y.; Liu, Z.; Yan, B.; Wang, D.; Huang, Z.; Li, X.; Fan, J.; Zhi, C. Do Zinc Dendrites Exist in Neutral Zinc Batteries: A Developed Electrohealing Strategy to In Situ Rescue In-Service Batteries. *Adv. Mater.* **2019**, *31*, 1903778.

(14) Hou, Z.; Gao, Y.; Tan, H.; Zhang, B. Realizing high-power and high-capacity zinc/sodium metal anodes through interfacial chemistry regulation. *Nat. Commun.* **2021**, *12* (1), 3083.

(15) Zuo, Y.; Wang, K.; Pei, P.; Wei, M.; Liu, X.; Xiao, Y.; Zhang, P. Zinc dendrite growth and inhibition strategies. *Materials Today Energy* **2021**, *20*, 100692.

(16) Li, M.; Li, Z.; Wang, X.; Meng, J.; Liu, X.; Wu, B.; Han, C.; Mai, L. Comprehensive understanding of the roles of water molecules in aqueous Zn-ion batteries: from electrolytes to electrode materials. *Energy Environ. Sci.* **2021**, *14* (7), 3796−3839.

(17) Guo, X.; Zhang, Z.; Li, J.; Luo, N.; Chai, G.-L.; Miller, T.-S.; Lai, F.; Shearing, P.; Brett, D. J. L.; Han, D.; Weng, Z.; He, G.; Parkin, I. P. Alleviation of Dendrite Formation on Zinc Anodes via Electrolyte Additives. *ACS Energy Lett.* **2021**, *6* (2), 395−403.

(18) Lu, W.; Zhang, C.; Zhang, H.; Li, X. Anode for Zinc-Based Batteries: Challenges, Strategies, and Prospects. *ACS Energy Lett.* **2021**, *6* (8), 2765−2785.

(19) Li, C.; Xie, X.; Liang, S.; Zhou, J. Issues and Future Perspective on Zinc Metal Anode for Rechargeable Aqueous Zinc-ion Batteries. *Energy Environ. Mater.* **2020**, *3* (2), 146−159.

(20) Zeng, Y.; Zhang, X.; Qin, R.; Liu, X.; Fang, P.; Zheng, D.; Tong, Y.; Lu, X. Dendrite-Free Zinc Deposition Induced by Multifunctional CNT Frameworks for Stable Flexible Zn-Ion Batteries. *Adv. Mater.* **2019**, *31* (36), 1903675.

(21) Zhang, Q.; Luan, J.; Fu, L.; Wu, S.; Tang, Y.; Ji, X.; Wang, H. The Three-Dimensional Dendrite-Free Zinc Anode on a Copper Mesh with a Zinc-Oriented Polyacrylamide Electrolyte Additive. *Angew. Chem., Int. Ed.* **2019**, *58* (44), 15841−15847.

(22) Wang, F.; Borodin, O.; Gao, T.; Fan, X.; Sun, W.; Han, F.; Faraone, A.; Dura, J. A.; Xu, K.; Wang, C. Highly reversible zinc metal anode for aqueous batteries. *Nat. Mater.* **2018**, *17* (6), 543−549.

(23) Sun, P.; Ma, L.; Zhou, W.; Qiu, M.; Wang, Z.; Chao, D.; Mai, W. Simultaneous Regulation on Solvation Shell and Electrode Interface for Dendrite-Free Zn Ion Batteries Achieved by a Low-Cost Glucose Additive. *Angew. Chem., Int. Ed.* **2021**, *60*, 18247.

(24) Tang, Y.; Liu, C.; Zhu, H.; Xie, X.; Gao, J.; Deng, C.; Han, M.; Liang, S.; Zhou, J. Ion-confinement effect enabled by gel electrolyte for highly reversible dendrite-free zinc metal anode. *Energy Stor. Mater.* **2020**, *27*, 109−116.

(25) Geng, L.; Wang, X.; Han, K.; Hu, P.; Zhou, L.; Zhao, Y.; Luo, W.; Mai, L. Eutectic Electrolytes in Advanced Metal-Ion Batteries. *ACS Energy Lett.* **2022**, *7* (1), 247−260.

(26) Zhao, Z.; Zhao, J.; Hu, Z.; Li, J.; Li, J.; Zhang, Y.; Wang, C.; Cui, G. Long-life and deeply rechargeable aqueous Zn anodes enabled by a multifunctional brightener-inspired interphase. *Energy Environ. Sci.* **2019**, *12* (6), 1938−1949.

(27) Shen, C.; Li, X.; Li, N.; Xie, K.; Wang, J. G.; Liu, X.; Wei, B. Graphene-Boosted, High-Performance Aqueous Zn-Ion Battery. *ACS Appl. Mater. Interfaces* **2018**, *10* (30), 25446−25453.

(28) Cui, M.; Xiao, Y.; Kang, L.; Du, W.; Gao, Y.; Sun, X.; Zhou, Y.; Li, X.; Li, H.; Jiang, F.; Zhi, C. Quasi-Isolated Au Particles as Heterogeneous Seeds to Guide Uniform Zn Deposition for Aqueous Zinc-Ion Batteries. *ACS Appl. Energy Mater.* **2019**, *2* (9), 6490−6496.

(29) Xie, X.; Liang, S.; Gao, J.; Guo, S.; Guo, J.; Wang, C.; Xu, G.; Wu, X.; Chen, G.; Zhou, J. Manipulating the ion-transfer kinetics and interface stability for high-performance zinc metal anodes. *Energy Environ. Sci.* **2020**, *13* (2), 503−510.

(30) Zhao, R.; Yang, Y.; Liu, G.; Zhu, R.; Huang, J.; Chen, Z.; Gao, Z.; Chen, X.; Qie, L. Redirected Zn Electrodeposition by an Anti-Corrosion Elastic Constraint for Highly Reversible Zn Anodes. *Adv. Funct. Mater.* **2021**, *31* (2), 2001867.

(31) Cui, J.; Li, Z.; Xu, A.; Li, J.; Shao, M. Confinement of Zinc Salt in Ultrathin Heterogeneous Film to Stabilize Zinc Metal Anode. *Small* **2021**, *17* (28), 2100722.

(32) Cui, Y.; Zhao, Q.; Wu, X.; Chen, X.; Yang, J.; Wang, Y.; Qin, R.; Ding, S.; Song, Y.; Wu, J.; et al. An Interface-Bridged Organic-Inorganic Layer that Suppresses Dendrite Formation and Side Reactions for Ultra-Long-Life Aqueous Zinc Metal Anodes. *Angew. Chem., Int. Ed.* **2020**, *59* (38), 16594−16601.

(33) Zheng, M.; Lian, F.; Zhu, Y.; Zhang, Y.; Liu, B.; Zhang, L.; Zheng, B. pH-responsive poly (xanthan gum-g-acrylamide-g-acrylic acid) hydrogel: Preparation, characterization, and application. *Carbohydr. Polym.* **2019**, *210*, 38−46.

(34) Chen, P.; Lang, J.; Zhou, Y.; Khlyustova, A.; Zhang, Z.; Ma, X.; Liu, S.; Cheng, Y.; Yang, R. An imidazolium-based zwitterionic polymer for antiviral and antibacterial dual functional coatings. *Sci. Adv.* **2022**, *8* (2), eabl8812.

(35) Zou, K.; Cai, P.; Deng, X.; Wang, B.; Liu, C.; Luo, Z.; Lou, X.; Hou, H.; Zou, G.; Ji, X. Highly stable zinc metal anode enabled by oxygen functional groups for advanced Zn-ion supercapacitors. *Chem. Commun.* **2021**, *57* (4), 528−531.

(36) Zhou, S.; Wang, Y.; Lu, H.; Zhang, Y.; Fu, C.; Usman, I.; Liu, Z.; Feng, M.; Fang, G.; Cao, X.; Liang, S.; Pan, A. Anti-Corrosive and Zn-Ion-Regulating Composite Interlayer Enabling Long-Life Zn Metal Anodes. *Adv. Funct. Mater.* **2021**, *31* (46), 2104361.

(37) Abdallah, M. Ethoxylated fatty alcohols as corrosion inhibitors for dissolution of zinc in hydrochloric acid. *Corros. Sci.* **2003**, *45* (12), 2705−2716.

(38) Hao, J.; Meng, T.; Shu, D.; Song, X.; Cheng, H.; Li, B.; Zhou, X.; Zhang, F.; Li, Z.; He, C. Synthesis of three dimensional N&S co-doped rGO foam with high capacity and long cycling stability for supercapacitors. *J. Colloid Interface Sci.* **2019**, *537*, 57−65.

(39) Cao, P.; Zhou, X.; Wei, A.; Meng, Q.; Ye, H.; Liu, W.; Tang, J.; Yang, J. Fast-Charging and Ultrahigh-Capacity Zinc Metal Anode for High-Performance Aqueous Zinc-Ion Batteries. *Adv. Funct. Mater.* **2021**, *31* (20), 2100398.

(40) Lan, C. J.; Lee, C. Y.; Chin, T. S. Tetra-alkyl ammonium hydroxides as inhibitors of Zn dendrite in Zn-based secondary batteries. *Electrochim. Acta* **2007**, *52* (17), 5407−5416.

(41) Zhang, Q.; Xia, K.; Ma, Y.; Lu, Y.; Li, L.; Liang, J.; Chou, S.; Chen, J. Chaotropic Anion and Fast-Kinetics Cathode Enabling Low-Temperature Aqueous Zn Batteries. *ACS Energy Lett.* **2021**, *6* (8), 2704−2712.

(42) Pan, H.; Shao, Y.; Yan, P.; Cheng, Y.; Han, K. S.; Nie, Z.; Wang, C.; Yang, J.; Li, X.; Bhattacharya, P.; Mueller, K. T.; Liu, J. Reversible aqueous zinc/manganese oxide energy storage from conversion reactions. *Nat. Energy* **2016**, *1* (5), 16039.

(43) Deng, Y.-P.; Liang, R.; Jiang, G.; Jiang, Y.; Yu, A.; Chen, Z. The Current State of Aqueous Zn-Based Rechargeable Batteries. *ACS Energy Lett.* **2020**, *5* (5), 1665−1675.